

Symmetry-controlled edge states in graphene-like topological sonic crystal

Zhang-Zhao Yang(杨彰昭), Jin-Heng Chen(陈晋恒), Yao-Yin Peng(彭尧吟), Xin-Ye Zou(邹欣晔)

Citation: Chin. Phys. B . 2020, 29(10): 104302 . **doi:** 10.1088/1674-1056/ab9c0e
Journal homepage: http://cpb.iphy.ac.cn; http://iopscience.iop.org/cpb

What follows is a list of articles you may be interested in

Ultrasonic beam focusing characteristics of shear-vertical waves for contact-type linear phased array in solid

Yu-Xiang Dai(戴宇翔), Shou-Guo Yan(阎守国), Bi-Xing Zhang(张碧星)

Chin. Phys. B . 2020, 29(3): 034304 . **doi:** 10.1088/1674-1056/ab69ed

Micro-crack detection of nonlinear Lamb wave propagation in three-dimensional plates with mixed-frequency excitation

Wei-Guang Zhu(祝伟光), Yi-Feng Li(李义丰), Li-Qiang Guan(关立强), Xi-Li Wan(万夕里), Hui-Yang Yu(余辉洋), Xiao-Zhou Liu(刘晓宙)

Chin. Phys. B . 2020, 29(1): 014302 . **doi:** 10.1088/1674-1056/ab5931

Simulation of acoustic fields emitted by ultrasonic phased array in austenitic steel weld

Zhong-Cun Guo(郭忠存), Shou-Guo Yan(阎守国), Bi-Xing Zhang(张碧星)

Chin. Phys. B . 2019, 28(11): 114302 . **doi:** 10.1088/1674-1056/ab4d41

Lamb waves topological imaging combining with Green's function retrieval theory to detect near filed defects in isotropic plates

Hui Zhang(张辉), Hai-Yan Zhang(张海燕), Meng-Yun Xu(徐梦云), Guo-Peng Fan(范国鹏), Wen-Fa Zhu(朱文发), Xiao-Dong Chai(柴晓冬)

Chin. Phys. B . 2019, 28(7): 074301 . **doi:** 10.1088/1674-1056/28/7/074301

Seismoelectric wave propagation modeling in a borehole in water-saturated porous medium having an electrochemical interface

Hao-Ran Ding(丁浩然), Jin-Xia Liu(刘金霞), Zhi-Wen Cui(崔志文), Tribikram Kundu

Chin. Phys. B . 2017, 26(12): 124301 . **doi:** 10.1088/1674-1056/26/12/124301

Symmetry-controlled edge states in graphene-like topological sonic crystal*

Zhang-Zhao Yang(杨彰昭)[1], Jin-Heng Chen(陈晋恒)[1], Yao-Yin Peng(彭尧吟)[1], and Xin-Ye Zou(邹欣晔)[1,2,†]

[1] *Key Laboratory of Modern Acoustics (MOE), Institute of Acoustics, Department of Physics, Collaborative Innovation Center of Advanced Microstructures, Nanjing University, Nanjing* 210093, *China*

[2] *State Key Laboratory of Acoustics, Institute of Acoustics, Chinese Academy of Sciences, Beijing* 100190, *China*

(Received 11 April 2020; revised manuscript received 23 May 2020; accepted manuscript online 12 June 2020)

Unique topological states emerged in various topological insulators (TI) have been proved with great application value for robust wave regulation. In this work, we demonstrate the parity inversion related to the definition of the primitive cell in one common lattice, and realize a type of symmetry-controlled edge states confined on the zigzag interfaces of the graphene-like sonic topological crystal. By simply sliding the selected 'layer' near the interface, the coupling of the pseudospin states induced by the multiple scattering for the C_{6v} lattice results in the adjustment of the edge states. Based on the physics of the states, we experimentally propose a prototype of acoustic topological filter hosting multiple channels with independent adjustable edge states and realize the selective high transmission. Our work diversifies the prospects for the applications of the gapped edge states in the robust wave regulation, and proposes a frame to design new topological devices.

Keywords: acoustic higher-order topological insulator, acoustic filter, controllable edge states

PACS: 43.20.+g, 43.35.+d, 52.35.Dm **DOI:** 10.1088/1674-1056/ab9c0e

1. Introduction

The concept of topological insulator (TI) has drawn extensive attention since it was proposed. In condensed matter physics, TI has been proved to be an excellent platform for new types of lossless information transmission because of its defects-immune property based on gapless topological-protected edge states.[1–5] In recent years, optical TIs[6–16] and acoustic TIs[17–26] have also been successfully demonstrated. More recently, the concept of higher-order topological insulator (HOTI) hosting gapped edge states and corner states has shown that the traditional bulk–boundary correspondence is no longer applicable to it.[27–34] Different from the topological phases of the traditional TIs, the reported works have shown that the topologies of the HOTIs are characterized by the nonzero bulk polarization, which are strongly related to the point group symmetry (PGS) of the periodic structures.[27,34–36] Moreover, some works have demonstrated that HOTIs can also be implemented in two-dimensional elastic waves,[37,38] microwaves,[39] toroidal circuits,[40] optical[41–44] and acoustic systems.[45–49]

The previous researches on the HOTIs have always focus on the 0D corner states which are capable of confining the energy on the corners exactly, however, we note that the normally-gapped edge states of the HOTIs also provide unprecedented platforms for the control of wave propagation. In the classical wave systems, the behaviors of the topological states crucially depend on the structure parameters of the material, which implies the possibilities to adjust the bands of the gapped edge states.

In this work, we propose a graphene-like sonic HOTI and focus on the behaviors of the edge states. We show that the parity inversion of the proposed HOTI depends on the choices of the primitive cells, and the inverted parities of the eigenstates at the high symmetry points near the nontrivial gaps, which indicate nonzero bulk polarization, lead to the generation of the edge states on the interface. Meanwhile, the pseudo-spins carried by the states originating from the graphene-like lattice ensure the robust wave propagation. Importantly, we further demonstrate that the translation of the 'layer' leads to the changing of the coupling strength of the multipolar states between the layers, and then results in the expansion or contraction of the gapped edge states. It indicates that the edge states can be adjusted by simply controlling the translation rates. Based on these, a prototype of two-dimensional acoustic topological filter with adjustable edge states is experimentally proposed. By simply sliding the sections of the filter, the bandwidths of the edge states can be controlled, and the propagation of the sound waves at specific frequencies band to the selected ports can be freely manipulated.

*Project supported by the National Key R&D Program of China (Grant No. 2017YFA0303700), the National Natural Science Foundation of China (Grant Nos. 11634006, 11934009, and 11690030), the Natural Science Foundation of Jiangsu Province, China (Grant No. BK20191245), the Fundamental Research Funds for the Central Universities, China (Grant No. 020414380131), and the State Key Laboratory of Acoustics, Chinese Academy of Sciences.

†Corresponding author. E-mail: xyzou@nju.edu.cn

© 2020 Chinese Physical Society and IOP Publishing Ltd

2. The creation of parity inversion

We start with a regular 2D SC with a C_{6v} symmetry lattice consisting of solid hexagonal columns embedded in the air background as shown in Fig. 1(a). The side length of the column is $r_0 = 6$ mm, and the distance between the nearest-neighbor columns is $R = 2.778r_0$. The lattice constant is $a = \sqrt{3}R$. In the perspective of HOTI, the nontrivial topology is determined by the bulk polarization, which in turn results in the emergence of the edge polarization (P_x, P_y). A nontrivial edge polarization indicates the existence of the in-gap edge states located on the boundaries of the nontrivial domains, and the robust 0D topological corner state can also emerge on the specific corner as the intersected boundaries are all polarized, which are different from the ordinary defects.[50–52] Meanwhile, the topology of the material is strongly related to the point group symmetry, which means that the parity inversion indicating the topological phase transition may be induced simply by selecting different definition of the unit cell in one common lattice.[53] In our work, the solid columns can be treated as hard boundries and the energy is actually propagating in the background air, which is different from the previous works.[24,49] To simplify the model of our work, we only consider two nearest-neighbor hoppings of the aerial meta-atoms respectively along x and y directions, and the structure can then be redefined with two types of rectangular supercells [red dashed lines in Fig. 1(a)]. Figures 1(b) and 1(c) depict the energy band structures of the two supercells, respectively. Due to the same lattice constants $a_x = a$, $a_y = \sqrt{3}a$, and the same periods along both directions, the energy band structures of the two supercells shall also be the same. However, the parity of the modal distribution of each band labeled with "+" (even parity) and "−" (odd parity) at the high symmetry points represents distinct topology.

The topological non-triviality of the parity inversion can be characterized by the integration of the Berry connection over the 1st BZ[27]

$$P_i = \frac{1}{(2\pi)^2}\iint \mathrm{d}^2k \mathrm{Tr}[A_i],$$
$$(A_i)_{mn}(k) = \mathrm{i}\left\langle u_m(k)\left|\partial_{k_i}\right|u_n(k)\right\rangle, \quad (1)$$

where i indicates the component of 2D polarization P along the reciprocal vector b_i, and $|u_m(k)\rangle$ is the periodic Bloch function for the m-th band. If applying C_2 rotation to this system, equation (1) can be rewritten as[36]

$$P_i = \frac{1}{2}\left(\sum_m q_i^m \bmod 2\right), \quad (2)$$
$$(-1)^{q_i^m} = \frac{\eta_m(M)}{\eta_m(\Gamma)}, \quad (3)$$

where $\eta_m(M)$ represents the parity at M point for the m-th band, and the summation runs over all occupied bands. According to the parities of the modes of the bands at the corresponding high symmetry points, the band gaps of the supercell 1 carry trivial topology, but the gaps of the supercell 2 carry nontrivial topology. To explain it exactly, we present the first four eigenmodes at M point of the two supercells in Figs. 1(d) and 1(e), respectively. The four parities of supercell 1 from bottom to top are characterized as s mode (+), d_{xy} mode (+), and a pair of p modes (−). Contrary, the corresponding parities of supercell 2 are a pair of p modes (−), s mode (+), and d_{xy} mode (+). The topology characterized by the inverted parities demonstrates the emergence of the higher-order topological states on the interfaces between the trivial and nontrivial domains.

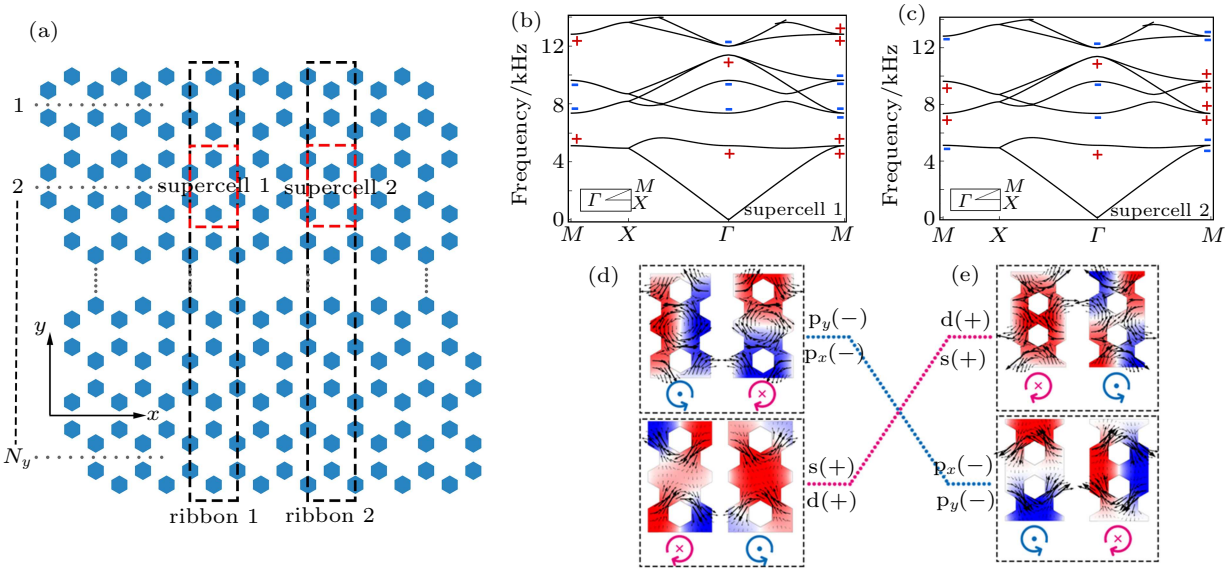


Fig. 1. (a) Schematic of two selected supercells (red dashed lines) based on one common graphene-like lattice, the corners and the edges of the supercells represent the pseudo-atoms and the corresponding hoppings, respectively. The corresponding energy band structures labeled with parities are presented in (b) and (c). (d) and (e) The pressure field distributions of the first two double-degenerate bands from bottom to top at M point of the two supercells, respectively. The opposite parities indicate the parity inversion.

Before introducing the topological states in this crystal, it is important to note that the nontrivial polarization of the domain does not require either the spin-like degrees of freedom or the time-reversal relation.[53,54] However, the pseudo-spins can still be introduced by multiple scattering for the special C_{6v} lattice.[24] We calculate the real-space distributions of the root-mean-square intensity of the energy flow $I = \frac{1}{T}\int \mathrm{Re}(p)\mathrm{Re}(v)\mathrm{d}t$ to describe the pseudo-spins in the two supercells as illustrated in Figs. 1(d) and 1(e) (see details in Appendix A). Crucially, the chiral flows on each corresponding band of the two supercells imply the promotion of the wave propagation between the domains with distinct topology.

3. Pseudo-spin-protected adjustable edge states

The bulk–edge–corner correspondence of the HOTIs predicts both the edge and corner states. In this work, we focus on the behaviors of the gapped edge states. Figures 2(a) and 2(b) present the energy band structures of two ribbons, which are periodic along y direction, composed of 30 trivial supercells or 15 trivial and 15 nontrivial supercells along x direction, respectively. Apparently, the predicted edge states vanish on the edge of the complete trivial domain [Fig. 2(a)], but emerge on the nontrivial interface and span the band gaps [Fig. 2(b)]. Meanwhile, due to the strong coupling of the pseudo-spins on the interface, the edge states appear to be gapless (see Fig. A2 in Appendix A).

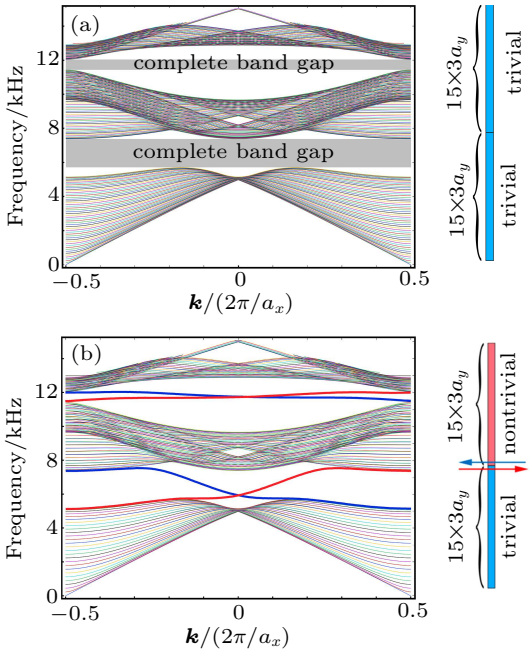


Fig. 2. Band structures of the ribbons composed of (a) 30 trivial supercells and (b) 15 trivial and 15 nontrivial supercells, being finite along y direction and periodic along x direction.

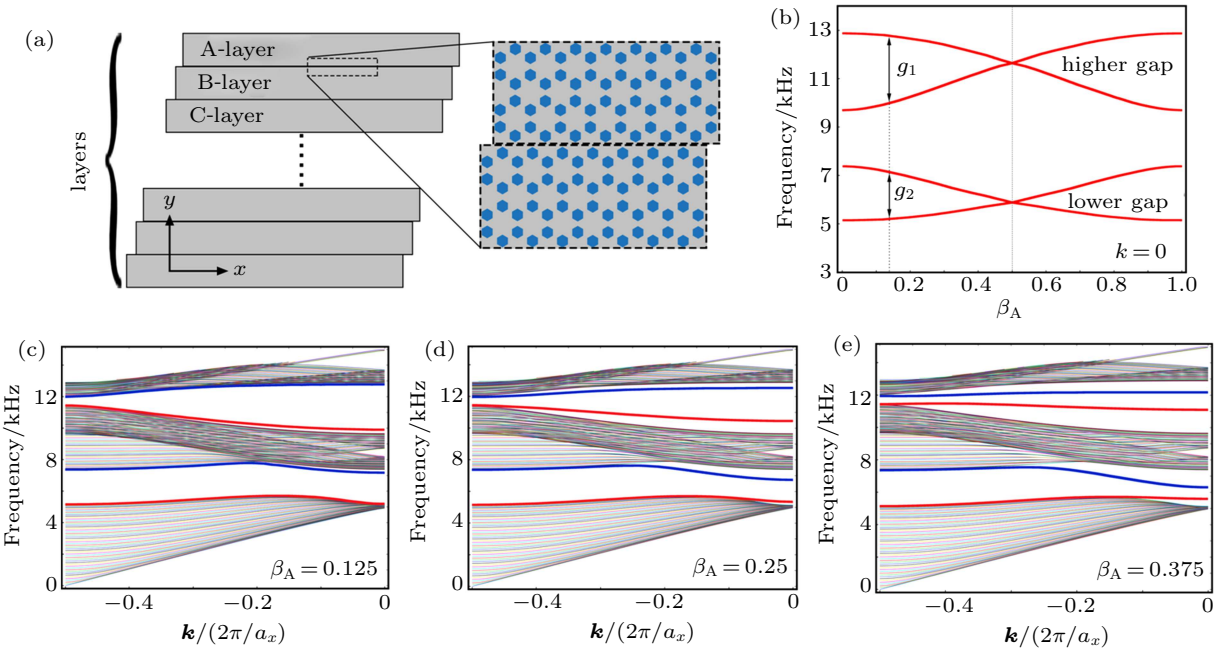


Fig. 3. (a) Schematic of the structure divided into independent layers. Inset: Details of the configuration near the interface. (b) β_A-dependent band-edge frequencies for the supercells with $k = 0$ within a translation period. g_1 and g_2 represent the ranges between the two topological bands. Energy band structures with distinct edge states for (c) $\beta_A = 0.125$, (d) 0.25, and (e) 0.375, respectively.

We emphasize that the two primitive cells with distinct topology corresponding to the same lattice, which implies that the band inversion can be induced by simply sliding the parts of the structure. As shown in Fig. 3(a), the structure is divided into layers, which can be slid along x direction independently. We define the translation rate $\beta_i = r_i/a_x$ (i = A, B, C, ...), where r_i indicates the actual amount of the translation of the i-th layer. We first study one interface between A-layer and B-layer [inset in Fig. 3(a)], and only consider the slide of A-layer. Figure 3(b) illustrates the correlation between the gap of the edge states and β_A. As β_A increases, the symmetry of the interface reduces and the coupling of the pseudo-

spins strengthens, which results in the expansion of the edge states. When $\beta_A = 0.5$, the anti-symmetry of the interface corresponds to the strongest coupling of the pseudo-spins, which meets the parity inversion exactly. Therefore, the edge states are steep and different from the flat cases without considering pseudo-spins.[36] Figures 3(c)–3(e) present the corresponding band structures for β_A being 0.125, 0.25, and 0.375, respectively.

We further consider three independent layers with $\beta_A = 0.5$, $\beta_C = 0.25$, and $\beta_B = 0$. Figure 4(a) shows the energy band structure of the corresponding ribbon. Significantly, there are two pairs of edge states in each gap, which represents the independent topological propagating modes on the two interfaces, respectively. The real-space distributions and the flows of intensity of the pressure field for $k = \pm 0.05 \times 2\pi/a_x$ shown in Fig. 4(b) depict the predicted topological modes confined on the specific interface. These results provide the possibility to design a type of multi-channel topological acoustic waveguide to achieve filtering at specific frequencies.

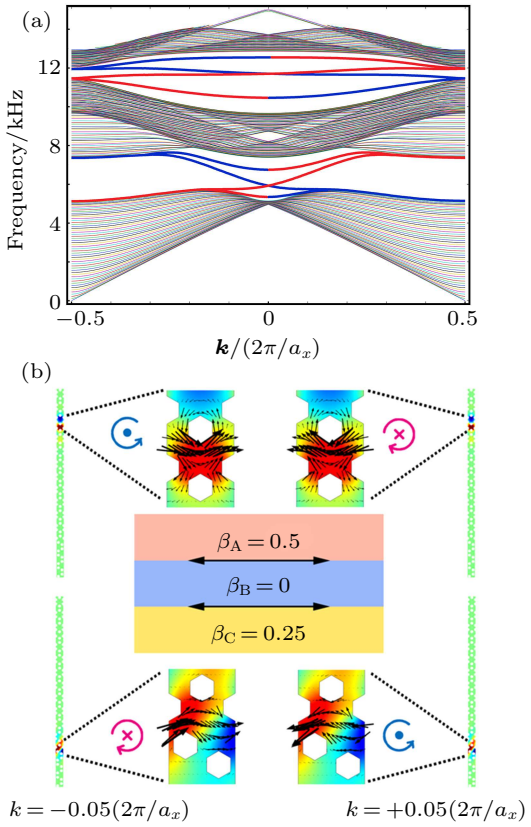


Fig. 4. (a) Energy band structure of the ribbon with two independent interfaces, the two pairs of the edge states are independently emerging on the specific interface. (b) Pressure field distributions and intensity flows of the pseudo-spin-dependent edge states for $k = \pm 0.05 \times 2\pi/a_x$ on the interfaces of the ribbon.

4. Experiments

Here, we construct a prototype of two-dimensional acoustic topological filter based on the crystal proposed above and experimentally measure the corresponding sound wave transmission. As shown in Fig. 5(a), the filter is composed of 3D printed solid hexagonal columns, which can be treated as the acoustic hard boundaries. The whole structure is placed between two hard-boundary waveguide plates to prevent the possible sound energy from leaking into the free space, and is surrounded by sound absorption boundaries to eliminate the interference of the environmental noise. The filter is divided into the four sections labeled with A, B, C, and D, and the four ports are labeled as input, port 2, port 3, and port 4 corresponding to the four inter-paths labeled with P_1, P_2, P_3, and P_4, respectively. A broadband sound source is placed at the input, and three transducers are placed at the other three ports to detect the sound energy transmission. We introduce the translation rates β_{P_i} $(i = 1, 2, 3, 4)$ to indicate the translation ratio of the corresponding path. If we set $\beta_{P_2} = \beta_{P_4} = 0$ and $\beta_{P_1} = \beta_{P_3} = 0.25$, the symmetry of the structure at P_1 and P_3 will be broken and two transport paths will be generated, which means that the sound wave can only propagate in one dimension. Figure 5(b) exhibits the high transmission of the

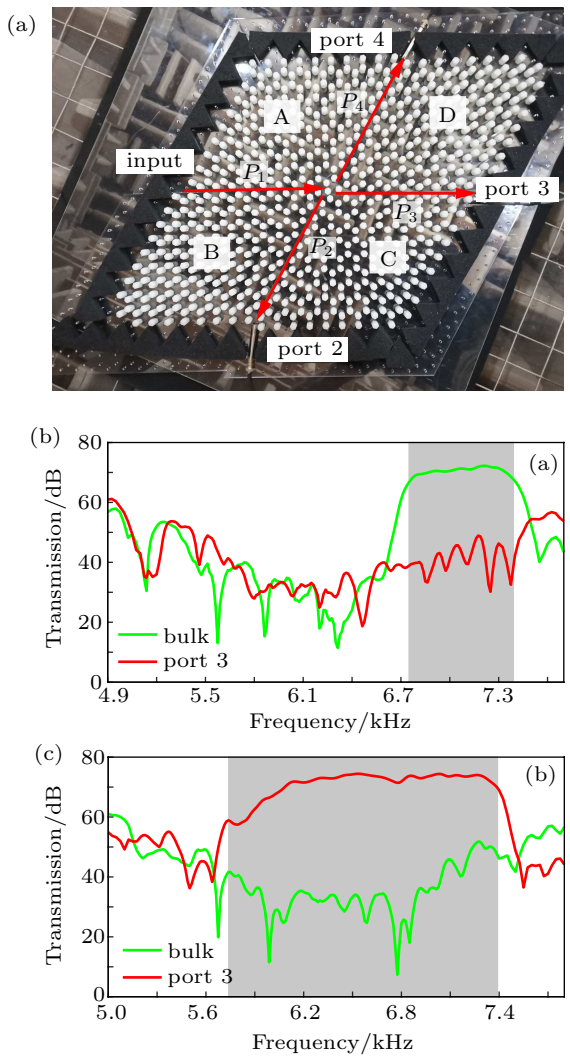


Fig. 5. (a) Experimental setup of the two-dimensional acoustic topological filter. (b) Measured bulk (green) and port 3 (red) transmission spectra for $\beta_{P_1} = \beta_{P_3} = 0.25$. (c) Measured bulk (green) and port 3 (red) transmission spectra for $\beta_{P_1} = \beta_{P_3} = 0.5$. The gray regions in both (b) and (c) represent the theoretic range of the edge states.

sound wave at 6.75–7.39 kHz to port 3 with very low leakage of the energy into the bulk, which corresponds to the energy band structure shown in Fig. 3(d). If β_{P_1} and β_{P_3} are increased to 0.5, the symmetry is the weakest and the sections on both sides are antisymmetric along the path. Hence, the two edge states in the band gaps connect to each other. Figure 5(c) shows the high-transmission of the sound wave at 5.74–7.39 kHz, which corresponds to the energy band structure shown in Fig. 2(b). These results experimentally demonstrate the adjustable edge states hosted by the filter.

We further study the two-dimensional transmission of the sound wave in the filter. Figure 6(a) shows the low transmission of the filter's three ports for $\beta_{P_i} = 0$ $(i = 1,2,3,4)$. If we set $\beta_{P_1} = \beta_{P_3} = 0.5$ and $\beta_{P_2} = \beta_{P_4} = 0.25$, the four transport paths will all be opened, but only P_1 and P_3 are antisymmetric. The corresponding transmissions illustrated in Fig. 6(b) indicate that the sound waves from 5.74 kHz to 6.75 kHz can only propagate along P_1 and P_3, but are hindered within P_2 and P_4. We show the numerical results of the energy fields for 6400 Hz and 7125 Hz in Figs. 6(c) and 6(d), respectively. Moreover, the total transmission efficiency of the three ports of the filter is almost 100% [dashed line in Fig. 6(b)] if the energy loss of the leakage or viscosity is ignored, which is consistent with the inherent property of TIs. Crucially, the independent translations in two directions indicate that the bandwidth of the edge states on the selected path can be adjusted freely. Therefore, an acoustic topological filter with multiple transmission channels can also be proposed by simply sliding the specific sections. In addition, it is noted that the filter is robust and topological protected, which is distinct from the ordinary defects.[55,56] Simulated results are given in Appendix B. This significant property to freely adjust the bandwidth of the edge states provides excellent ways for the design of adjustable topological acoustic materials.

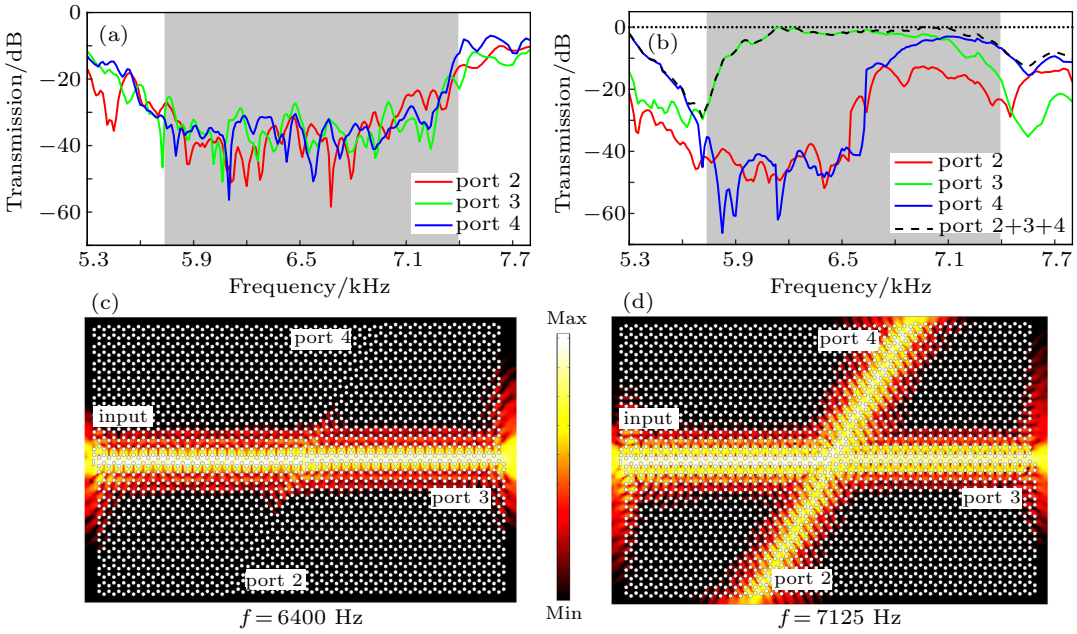


Fig. 6. (a) Measured transmission spectra for port 2 (red), port 3 (green), and port 4 (blue) when $\beta_{P_i} = 0$. (b) Measured transmission spectra for port 2 (red), port 3 (green), port 4 (blue) and the sum of the three ports for $\beta_{P_1} = \beta_{P_3} = 0.5$ and $\beta_{P_2} = \beta_{P_4} = 0.25$. The green dashed curve representing the total transmission loss exhibits lossless transmission in the two theoretical frequency ranges marked with grey. (c) and (d) The simulated acoustic energy transmission distributions for 6400 Hz and 7125 Hz, respectively.

5. Conclusion

We have numerically and experimentally demonstrated the adjustable edge states of the two-dimensional graphene-like sonic HOTI. By tuning the translation rate of the layers of the material, we can change the coupling strength of the pseudo-spins on the interface, and then control the gapped edge states. Besides, we have proposed a prototype of multi-channel topological filter with independent adjustable edge states, and experimentally demonstrated its almost lossless transmission of the acoustic waves. These results provide new perspective to control the edge states. Based on this work, we expect to expand the design of the topological insulators, and provide the novel application prospects of acoustic topological materials such as filters, waveguides, and acoustic switches.

Appendix A: The pseudo-spins in acoustic systems

For the acoustic waves, the in-plane velocity fields associated with the pressure fields $p_x(\boldsymbol{r})$ and $p_y(\boldsymbol{r})$ are given by the wave equation[24]

$$\boldsymbol{v}_1 = -\frac{\mathrm{i}}{\rho\omega}\left(\frac{\partial p_x}{\partial x}\hat{\boldsymbol{x}} + \frac{\partial p_y}{\partial y}\hat{\boldsymbol{y}}\right) = h_{1x}\hat{\boldsymbol{x}} + h_{1y}\hat{\boldsymbol{y}}, \tag{A1}$$

$$\boldsymbol{v}_2 = -\frac{\mathrm{i}}{\rho\omega}\left(\frac{\partial p_y}{\partial x}\hat{\boldsymbol{x}} + \frac{\partial p_y}{\partial y}\hat{\boldsymbol{y}}\right) = h_{2x}\hat{\boldsymbol{x}} + h_{2y}\hat{\boldsymbol{y}}. \tag{A2}$$

Equations (A1) and (A2) can be rewritten as $\boldsymbol{v}_i = h_{ix}\hat{\boldsymbol{x}} + h_{iy}\hat{\boldsymbol{y}}$ $(i = 1, 2)$, where $\hat{\boldsymbol{x}}$ and $\hat{\boldsymbol{y}}$ are the unit vectors. Since the wave functions of pressure field $p_x(\boldsymbol{r})$ and $p_y(\boldsymbol{r})$ are linked to each other by $\pi/2$ rotation, one has at origin

$$\begin{pmatrix} h_{2x} \\ h_{2y} \end{pmatrix} = \begin{pmatrix} h_{1y} \\ -h_{1x} \end{pmatrix}. \tag{A3}$$

The total velocity fields are obtained from

$$\begin{aligned} \boldsymbol{v} &= -\frac{\mathrm{i}}{\rho\omega}\nabla\left(p_x \pm \mathrm{i}p_y\right) = \left(h_{1x} \pm \mathrm{i}h_{2x}\right)\hat{\boldsymbol{x}} + \left(h_{1y} \pm \mathrm{i}h_{2y}\right)\hat{\boldsymbol{y}} \\ &= \left(h_{1x} \pm h_{1y}\right)\left(\hat{\boldsymbol{x}} \mp \mathrm{i}\hat{\boldsymbol{y}}\right). \end{aligned} \tag{A4}$$

A $\pm\pi/2$ phase shift in x and y components of velocity fields is obtained from the term $\pm\mathrm{i}$ in front of $\hat{\boldsymbol{y}}$ in Eq. (A4) because of the time harmonic mode $\exp(\mathrm{i}\omega t)$. This phase shift represents the circular polarization of the in-plane velocity fields, which corresponds to the angular momentum of the wave function of the pressure fields in the present SC. The circular polarization can be used to simulate acoustic pseudo-spin states. We show the pseudo-spin states in Fig. A1.

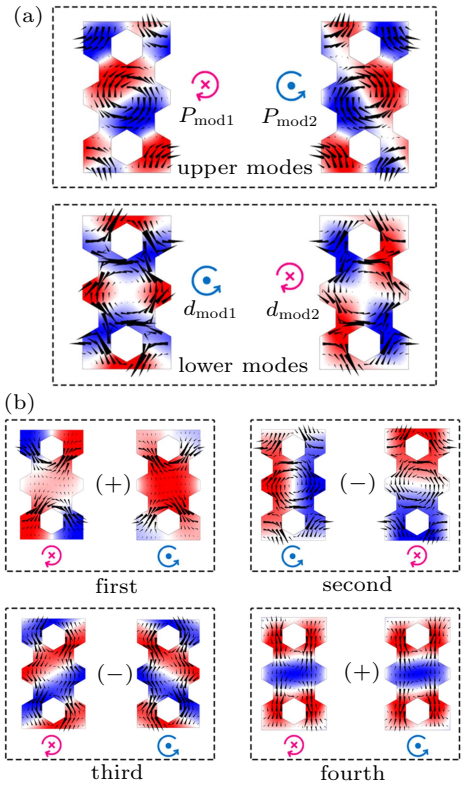


Fig. A1. Pseudo-spin states at (a) Γ and (b) M. In (a), $d_{\mathrm{mod}\,1,2}$ represents the double-degenerate modes below the upper gap at Γ, and $p_{\mathrm{mod}\,1,2}$ represents the modes upon the upper gap. In (b), the labels of the four dotted boxes represent the count of the double-degenerate bands from bottom to top. The $(\pm)$ represents the parity of each mode, and circulation arrow of energy flow demonstrates the certain pseudo-spin state. The relative band structure is shown in Fig. 3(b).

Moreover, we consider the two interface conditions: one is composed of the same material, and the other is composed of materials with distinct topology. The directions of the pseudo-spin in the former condition are all the same. In the latter condition, the pseudo-spin of the upper material is anti-clockwise and that of the lower material is clockwise. The corresponding interfaces are insulating and conductive, which can be illustrated by the symbolic equation "$0 = 1 - 1$" and "$2 = 1 + 1$", respectively. The schematic diagrams of the two condition are shown in Figs. A2(a) and A2(b), respectively.

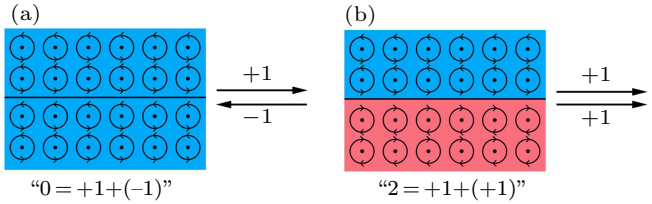


Fig. A2. Schematic diagrams of the two conditions: (a) the upper and the lower materials are the same and (b) the upper and the lower materials are different. The structure in (a) appears to be insulating, and the structure in (b) appears to be conductive.

Appendix B: Edge states vs. ordinary defects

An important character of the topological states is robust against defects. Here, we simulate the cases with a cavity or a disturbance on the nontrivial interface, compared with the ordinary defects, as illustrated in Figs. B1(a) and B1(b). The corresponding simulated transmission spectra for different cases are present in Fig. B1(c), which depicts the robustness and high transmission of the topological edge states.

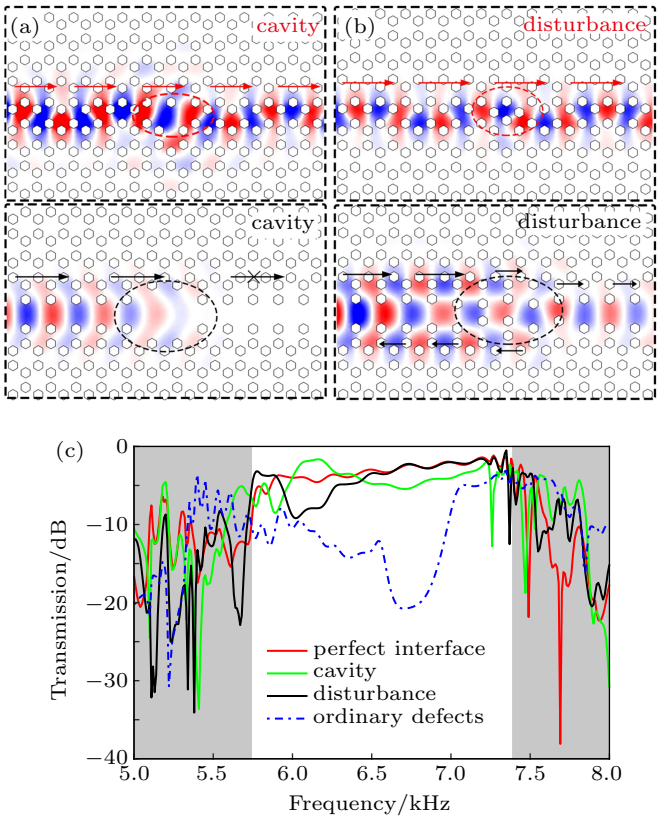


Fig. B1. Comparison of the simulated acoustic field distribution at 6.84 kHz for topological interface and ordinary defects, corresponding to (a) a cavity and (b) a disturbance in the waveguide. The red and black arrows represent propagation of the topological states and ordinary sound, respectively. (c) Simulated transmission spectra for perfect topological interface (red curve), topological interface with a cavity (green curve), topological interface with a disturbance (black curve) and ordinary defects (blue dashed curve). The white region represents the predicted range of edge states.

References

[1] Kane C L and Mele E J 2005 *Phys. Rev. Lett.* **95** 146802
[2] Kane C L and Mele E J 2005 *Phys. Rev. Lett.* **95** 226801
[3] Moore J E 2010 *Nature* **464** 194
[4] Hasan M Z and Kane C L 2010 *Rev. Mod. Phys.* **82** 3045
[5] Qi X and Zhang S C 2011 *Rev. Mod. Phys.* **83** 1057
[6] Haldane F D M and Raghu S 2008 *Phys. Rev. Lett.* **100** 013904
[7] Wang Z, Chong Y D, Joannopoulos J D and Soljačić M 2008 *Phys. Rev. Lett.* **100** 013905
[8] Hafezi M, Demler E A, Lukin M D and Taylor J M 2011 *Nat. Phys.* **7** 907
[9] Poo Y, Wu R, Lin Z, Yang Y and Chan C T 2011 *Phys. Rev. Lett.* **106** 093903
[10] Rechtsman M C, Zeuner J M, Plotnik Y, Lumer Y, Podolsky D, Dreisow F, Nolte S, Segev M and Szameit A 2013 *Nature* **496** 196
[11] Khanikaev A B, Mousavi S H, Tse W, Kargarian M, MacDonald A H and Shvets G 2013 *Nat. Mater.* **12** 233
[12] Liang G Q and Chong Y D 2013 *Phys. Rev. Lett.* **110** 203904
[13] Lu L, Joannopoulos J D and Soljačić M 2014 *Nat. Photon.* **8** 821
[14] Wu L and Hu X 2015 *Phys. Rev. Lett.* **114** 223901
[15] Khanikaev A B and Shvets G 2017 *Nat. Photon.* **11** 763
[16] Gao F, Xue H, Yang Z, Lai K, Yu Y, Lin X, Chong Y, Shvets G and Zhang B 2018 *Nat. Phys.* **14** 140
[17] Khanikaev A B, Fleury R, Mousavi S H and Alù A 2015 *Nat. Commun.* **6** 8260
[18] Xiao M, Chen W, He W and Chan C T 2015 *Nat. Phys.* **11** 920
[19] Yang Z, Gao F, Shi X, Lin X, Gao Z, Chong Y and Zhang B 2015 *Phys. Rev. Lett.* **114** 114301
[20] Fleury R, Khanikaev A B and Alù A 2016 *Nat. Commun.* **7** 11744
[21] Peng Y, Qin C, Zhao D, Shen Y, Xu X, Bao M, Jia H and Zhu X 2016 *Nat. Commun.* **7** 13368
[22] He C, Ni X, Ge H, Sun X, Chen Y, Lu M, Liu X and Chen Y 2016 *Nat. Phys.* **12** 1124
[23] Lu J, Qiu C, Ye L, Fan X, Ke M, Zhang F and Liu Z 2017 *Nat. Phys.* **13** 369
[24] Zhang Z, Wei Q, Cheng Y, Zhang T, Wu D and Liu X 2017 *Phys. Rev. Lett.* **118** 084303
[25] Lu J, Qiu C, Deng W, Huang X, Li F, Zhang F, Chen S and Liu Z 2018 *Phys. Rev. Lett.* **120** 116802
[26] Ding Y J, Peng Y G, Zhu Y F, Fan X D, Yang J, Liang B, Zhu X F, Wan X G and Cheng J C 2019 *Phys. Rev. Lett.* **122** 014302
[27] Fang C, Gilbert M J and Bernevig B A 2012 *Phys. Rev. B* **86** 115112
[28] Benalcazar W A, Bernevig B A and Hughes T L 2017 *Phys. Rev. B* **96** 245115
[29] Liu F and Wakabayashi K 2017 *Phys. Rev. Lett.* **118** 076803
[30] Langbehn J, Peng Y, Trifunovic L, von Oppen F and Brouwer P W 2017 *Phys. Rev. Lett.* **119** 246401
[31] Song Z, Fang Z and Fang C 2017 *Phys. Rev. Lett.* **119** 246402
[32] Benalcazar W A, Bernevig B A and Hughes T L 2017 *Science* **357** 61
[33] Ezawa M 2018 *Phys. Rev. Lett.* **120** 026801
[34] Liu F, Deng H and Wakabayashi K 2019 *Phys. Rev. Lett.* **122** 086804
[35] Liu F, Deng H and Wakabayashi K 2018 *Phys. Rev. B* **97** 035442
[36] Liu F, Yamamoto M and Wakabayashi K 2017 *J. Phys. Soc. Jpn.* **86** 123707
[37] Serra-Garcia M, Peri V, Süsstrunk R, Bilal O R, Larsen T, Villanueva L G and Huber S D 2018 *Nature* **555** 342
[38] Fan H, Xia B, Tong L, Zheng S and Yu D 2019 *Phys. Rev. Lett.* **122** 204301
[39] Peterson C W, Benalcazar W A, Hughes T L and Bahl G 2018 *Nature* **555** 346
[40] Imhof S, Berger C, Bayer F, Brehm J, Molenkamp L W, Kiessling T, Schindler F, Lee C H, Greiter M, Neupert T and Thomale R 2018 *Nat. Phys.* **14** 925
[41] Noh J, Benalcazar W A, Huang S, Collins M J, Chen K P, Hughes T L and Rechtsman M C 2018 *Nat. Photon.* **12** 408
[42] Xie B, Wang H, Wang H, Zhu X, Jiang J, Lu M and Chen Y 2018 *Phys. Rev. B* **98** 205147
[43] Mittal S, Orre V V, Zhu G, Gorlach M A, Poddubny A and Hafezi M 2019 *Nat. Photon.* **13** 692
[44] Li M, Zhirihin D, Gorlach M, Ni X, Filonov D, Slobozhanyuk A, Alù A and Khanikaev A B 2020 *Nat. Photon.* **14** 89
[45] Xue H, Yang Y, Gao F, Chong Y and Zhang B 2019 *Nat. Mater.* **18** 108
[46] Ni X, Weiner M, Alù A and Khanikaev A B 2019 *Nat. Mater.* **18** 113
[47] Zhang X, Wang H, Lin Z, Tian Y, Xie B, Lu M, Chen Y and Jiang J 2019 *Nat. Phys.* **15** 582
[48] Chen Z, Xu C, Al Jahdali R, Mei J and Wu Y 2019 *Phys. Rev. B* **100** 075120
[49] Zhang Z, Rosendo López M, Cheng Y, Liu X and Christensen J 2019 *Phys. Rev. Lett.* **122** 195501
[50] Yu S, Ni X, Xu Y, He C, Priyanka N, Lu M and Chen Y 2016 *Chin. Phys. Lett.* **33** 044302
[51] Khelif A, Choujaa A, Benchabane S, Djafari-rouhani B and Laude V 2004 *Appl. Phys. Lett.* **84** 4400
[52] Ahmet C, Olgun A K and Bulent U 2013 *Chin. Phys. B* **22** 114301
[53] Ota Y, Liu F, Katsumi R, Watanabe K, Wakabayashi K, Arakawa Y and Iwamoto S 2019 *Optica* **6** 786
[54] Ryo O, Shin H and Takeshi N 2019 *Phys. Rev. B* **100** 235302
[55] Kong X, Yue L, Chen Y and Liu Y 2012 *Chin. Phys. B* **21** 096101
[56] Fang Z and Hou Z 2018 *Chin. Phys. Lett.* **35** 054601